

Natural quantum reservoir computing for temporal information processing

Yudai Suzuki · Qi Gao · Ken Pradel · Kenji Yasuoka · Naoki Yamamoto

the date of receipt and acceptance should be inserted later

Abstract Reservoir computer is a temporal information processing system that exploits an artificial or physical dissipative dynamics to learn a dynamical system generating the target time-series. This paper proposes the use of real superconducting quantum computing devices as the reservoir, where the dissipative property is served by the natural noise added to the quantum bits. The performance of this natural quantum reservoir is demonstrated in a benchmark time-series regression problem and a practical problem classifying different objects based on a temporal sensor data. In both cases the proposed reservoir computer shows a higher performance than a linear regression or classification model. The results indicate that a noisy quantum device potentially functions as a reservoir computer, and

Y. Suzuki

Department of Mechanical Engineering, Keio University, Hiyoshi 3-14-1, Kohoku, Yokohama 223-8522, Japan

Q. Gao

Mitsubishi Chemical Corporation, Science & Innovation Center, 1000, Kamoshida-cho, Aoba-ku, Yokohama 227-8502, Japan

Quantum Computing Center, Keio University, Hiyoshi 3-14-1, Kohoku, Yokohama 223-8522, Japan

K. Pradel

Mitsubishi Chemical Corporation, Science & Innovation Center, 1000, Kamoshida-cho, Aoba-ku, Yokohama 227-8502, Japan

K. Yasuoka

Department of Mechanical Engineering, Keio University, Hiyoshi 3-14-1, Kohoku, Yokohama 223-8522, Japan

N. Yamamoto

Department of Applied Physics and Physico-Informatics, Keio University, Hiyoshi 3-14-1, Kohoku, Yokohama 223-8522, Japan

Quantum Computing Center, Keio University, Hiyoshi 3-14-1, Kohoku, Yokohama 223-8522, Japan

notably, the quantum noise, which is undesirable in the conventional quantum computation, can be used as a rich computation resource.

Keywords Reservoir computing · Natural quantum reservoir · Machine learning

1 Introduction

Recent remarkable advances in machine learning have attracted more and more attention in e.g., bioinformatics [1], computer visions [2,3], finance [4,5], and physics [6,7]. In fact, machine learning offers powerful and efficient techniques for solving various types of tasks appearing over those research areas. One of the common tasks is temporal information processing, where sequential or time-series data is processed to achieve a specific goal, such as natural language processing [8] and robotics [9]. To solve the temporal information tasks, recurrent neural network (RNN) [10], a neural network with recurrent structure, is often used. The basic strategy to train RNN is to recurrently connect the nodes, so that it approximates a target dynamical system, which is however computationally demanding.

As a special type of RNN, reservoir computing (RC) [11] has been actively studied, which are originated from echo state networks (ESNs) [12] and liquid state machines (LSMs) [13]. In RC, the temporal input data is mapped into the state of a high-dimensional dynamical system called the *reservoir*, and then the simple linear regression is used to adjust the weight of the readout signal of the dynamics, to approximate the target output signal. By virtue of this simple learning process, RC can realize fast and stable learning with less computational cost, compared to the typical RNNs.

Note that the reservoir serves as a nonlinear pattern mapping of the input signal to a high-dimensional dynamical states, as do kernel functions in kernel methods [14]. Thus, the choice of the type of reservoir systems to be implemented is of significant importance. In the last few decades, many different implementations of reservoirs have been proposed, from the original ESN and LSM models to *physical reservoir* such as field programmable gates arrays (FPGAs) [15], a bucket of water [16], soft robotics [17], tensegrity-structured robots [18], and spintronics [19]. Those physical reservoir implementation has attracted increasing attention, because physical reservoirs are possibly advantageous in faster information processing with low computational cost for learning and higher performance [20,21]. In this direction, quantum systems was proposed as a promising candidate for the physical reservoir [22]. This is because of the common thought that large quantum systems would be in general hard to simulate by classical computers, and thus the quantum reservoirs (QRs) with intrinsic complex dynamics are conjectured to show high performance for some temporal information tasks. In fact, the quantum reservoir computing (QRC) has been extensively investigated; the theoretical analysis of the QR property [23,24], the performance analysis through numerical simulations [25,26], various further improvement [27–29], and its applications to quantum tasks such as quantum tomography [30,31]. Also, thanks to the progress in quantum hardwares, the physical implementations of QRs have been demonstrated on the nuclear magnetic resonance (NMR) ensemble systems [32] and superconducting quantum processors [24].

In this paper, we propose a QRC framework that exploits a *natural* quantum dynamics on a gate-based superconducting quantum processors as a reservoir, for temporal information processing. This is in stark contrast to the previously developed *artificial* QRC architecture; that is, previously, the quantum dynamical system at each timestep is realized by injecting the inputs into one ancillary qubit and driving the whole QR system via an input-independent Hamiltonian, and finally discarding and resetting the ancillary qubit for the next step. The discard of the ancillary qubit in this process is crucial to realize the dissipative nature of the system, which is an essential property for reservoirs. On the other hand, in our QR systems, we instead utilize the intrinsic noise of the quantum devices for realizing a dissipative quantum dynamics. That is, we rather positively take advantage of the currently available noisy intermediate-scale quantum (NISQ) devices [33] which have inevitable dissipative noises (decoherence). The idea behind our proposal comes from the fact that the seemingly undesired behavior of dynamical systems could be a rich computational resource for the RC framework, such as the soft robot reservoir [17]. Note that, in this manuscript, we use the term *natural reservoir* to denote physical reservoir that is difficult to describe mathematically such as the dynamics of the soft robotics in [17], while the term *artificial reservoir* is used to denote the one whose mathematical model is in principle available.

The proposed natural QRC approach is a hardware-specific one, and its performance must be experimentally evaluated on a real device. In this work we utilize IBM superconducting quantum processors to demonstrate our QR systems for two temporal information tasks; emulation of the Nonlinear Auto-Regressive Moving Average dynamics (NARMA task) and classification of different objects based on the sensor-data obtained by grabbing them (object classification task). For NARMA task, we observed that our QR systems realized on 'ibmq_16_melbourne' (we simply call the Melbourne device) show higher performances than a linear regression model. As for the object classification task, our QR system on 'ibmq_toronto' (the Toronto device) shows higher classification accuracy than a simple linear classifier for the task of classifying three objects. These results indicate that a natural QR realized on a noisy quantum device can be added to promising candidates of reservoir for the RC framework. At the same time, this work will pave a new way for applying NISQ devices for solving practical problems.

2 Methods

2.1 General framework of reservoir computing

RC utilizes a dynamical system to execute temporal information processing tasks. Typically, the goal of this task is to learn a function that transforms an input sequence (time series) to a target output sequence, for the purpose of time series forecasting [34] and pattern classification [35]. In this work, we consider a given pair of scalar input signal $\{u_t\}_{t=1}^M$ and scalar output $\{y_t\}_{t=1}^M$. The RC model is described as follows;

$$x_t = f(x_{t-1}, u_t), \quad (1)$$

$$\bar{y}_t = W_{out}^T h(x_t), \quad (2)$$

where x_t is the state vector at time t and \bar{y}_t is the scalar output. W_{out} is the vector of adjustable parameters, which is to be optimized by a learning algorithm, so that \bar{y}_t approximates y_t . The function f represents the time evolution of the reservoir state x_t , driven by the input u_t , and h is a function that observes signals from x_t . The point of this RC framework is that the reservoir part is fixed unlike RNN, meaning that the learning

algorithm is much simpler than RNN. On the other hand, the crucial role of the feature extraction is left to the reservoir dynamics, hence the choice/design of reservoir is very important.

In RC framework, the parameters W_{out} is tuned in a supervised manner; the mean squared error (MSE) between the output \bar{y}_t and the target output y_t during the training phase, $MSE = \sum_{t=t_f}^{t_l} (\bar{y}_t - y_t)^2$, is minimized, where t_l and t_f are the last and first timestep of the training phase, respectively. This can be readily solved via the linear regression technique; the solution is given by the pseudo inverse of the linear equation

$$\mathbf{y} = W_{out}^T \mathbf{X}, \quad (3)$$

where $\mathbf{X} = (\tilde{h}(\mathbf{x}_{t_f}), \dots, \tilde{h}(\mathbf{x}_{t_l}))$ and $\mathbf{y} = (\bar{y}_{t_f}, \dots, \bar{y}_{t_l})$. Here $\tilde{h}(\cdot)$ is the vector containing both $h(\cdot)$ and the bias term 1, i.e. $\tilde{h}(\cdot) = (h(\cdot)^T, 1)^T$.

2.2 Quantum reservoir computing model

In the QRC framework, the dynamical system (1) is given by

$$\rho_t = \mathcal{T}_{u_t}(\rho_{t-1}), \quad (4)$$

where ρ_t is the density operator that represents a state of the QR at time t , and \mathcal{T}_{u_t} is an input-dependent completely positive and trace preserving (CPTP) map that describes the time evolution of the QR system. The CPTP map considered in Ref. [22] is given by

$$\begin{aligned} \rho_t &= \mathcal{T}_{u_t}(\rho_{t-1}) \\ &= e^{-iH\tau} (\rho_{\text{input}} \otimes \text{Tr}_{\text{input}}(\rho_{t-1})) e^{iH\tau}, \end{aligned} \quad (5)$$

where $\rho_{\text{input}} = |\psi_{u_t}\rangle\langle\psi_{u_t}|$ with $|\psi_{u_t}\rangle = \sqrt{1-u_t}|0\rangle\langle 0| + \sqrt{u_t}|1\rangle\langle 1|$. That is, the input $u_t \in [0, 1]$ is injected onto one ancillary qubit, and then the whole QR system is time-evolved by the input-independent unitary operator $e^{-iH\tau}$. The partial trace over the ancillary qubit, represented by Tr_{input} , is essential to have the dissipative property for QRC.

The function h in Eq. (2) is usually given by a set of the expectation values of local observables defined on the QR system. For an n -qubit QR system, we can take a set of the expectation values

$$h(\rho_t) = [\text{Tr}(Z_1\rho_t), \dots, \text{Tr}(Z_n\rho_t)]^T, \quad (6)$$

where Z_i is the Pauli Z matrix on the i th qubit, i.e.,

$$Z_i = I \otimes \dots \otimes Z \otimes \dots \otimes I, \quad Z = \begin{bmatrix} 1 & 0 \\ 0 & -1 \end{bmatrix}, \quad I = \begin{bmatrix} 1 & 0 \\ 0 & 1 \end{bmatrix}.$$

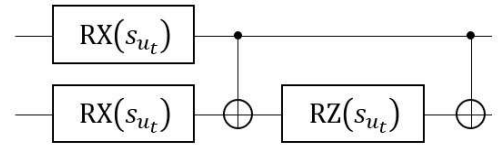


Fig. 1 Quantum circuit representation of the local 2 qubits unitary operator (9).

2.3 Natural quantum reservoir

Here we describe our QR system that, unlike the artificial mixing process Tr_{input} given in Eq. (5), makes full use of the natural noise as a computational resource for the QRC paradigm.

As mentioned in Section 1, the currently-available quantum devices must suffer from quantum noise. However, in the QRC framework, those unwanted quantum noise could be rather beneficial. For example, the QR system with depolarizing error can satisfy one of the essential properties of the reservoir, the echo-state property [36] or the convergence property [37], which is in a broad sense a condition that the system asymptotically forgets its initial state. To be more specific, the depolarizing error is given by the following CPTP map:

$$\mathcal{E}_{\text{dep}}(\rho) = (1-p)\rho + p\frac{I}{d},$$

where ρ is a system density matrix with the size of d and p is the parameter proportional to the probability that the quantum state becomes the maximally-mixed state [38]. The convergence property of the QR in this case can be easily checked; if the depolarizing channel is successively applied to the system, ρ asymptotically converges to the maximally-mixed state, I/d . In general, the dynamical system under unital error process converges to a stable equilibrium state [39, 40]. In addition, the QR system implemented on a noisy device potentially has a desirable "memory" property; in fact it was reported in [41] that a noisy quantum device has some memory effects such as temporal correlation. For these reasons, an open quantum system under natural error is potentially utilizable as a QR.

Based on the above discussion, we consider the following dynamics as the QR system (4):

$$\begin{aligned} \rho_t &= \mathcal{T}_{u_t}(\rho_{t-1}) \\ &= \mathcal{E}_{\text{device}}(U(u_t)\rho_{t-1}U(u_t)^\dagger), \end{aligned} \quad (7)$$

where $U(u_t)$ is an input-dependent unitary operator and $\mathcal{E}_{\text{device}}$ is the un-modeled CPTP map corresponding to the real device under operation. In this work, we consider the n -qubits system driven by the unitary operator

$$U(u_t) = \bar{U}_{0,1}(u_t) \otimes \bar{U}_{2,3}(u_t) \otimes \dots \otimes \bar{U}_{n-2,n-1}(u_t), \quad (8)$$

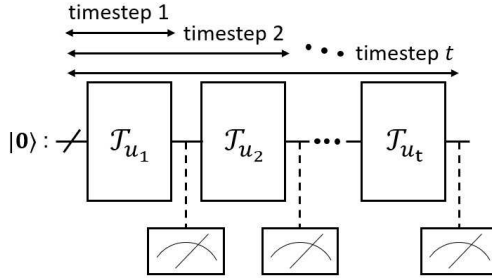


Fig. 2 Circuit diagram of the proposed QR system. $|0\rangle$ stands for the initial state, and \mathcal{T}_{u_i} is a fixed CPTP map with input u_i . The output signal (6) is obtained by repeatedly running the quantum circuit according to Eq. (10) and measuring Z for each qubit.

where $\bar{U}_{i,j}(u_t)$ is the identical local 2-qubits unitary operator acting on the i th and j th qubits:

$$\bar{U}_{i,j}(u_t) = \text{CX}_{i,j} \text{RZ}_j(s_{u_t}) \text{CX}_{i,j} \text{RX}_i(s_{u_t}) \text{RX}_j(s_{u_t}). \quad (9)$$

Here $s_{u_t} = au_t$ with $a \in \mathbb{R}$ and $\text{CX}_{i,j}$ is the CNOT gate with control qubit i and target qubit j . Also $\text{RZ}_i(s) = \exp(-isZ/2)$ and $\text{RX}_i(s) = \exp(-isX/2)$ are the rotation gate applied on the i th qubit, around Pauli Z and X axis, respectively. This 2-qubits unitary operator originates from [42], showing the effectiveness for another classification task. At $t = 0$, the state is prepared to $|0\rangle = H^{\otimes n} |0\rangle^{\otimes n}$ with H the Hadamard gate. The quantum circuit representation of the local unitary operator $\bar{U}_{i,j}(u_t)$ is depicted in Fig. 1. Note that, in the noiseless situation, Eq. (8) is a trivial dynamics composed of identical and independent 2-qubits subsystems. However, the subsystems implemented on a noisy real device may be able to couple with the neighboring subsystems due to the natural noise introduced from the surrounding environment, such as the crosstalk [43, 44], which as a result may lead to a non-trivial QR dynamics. Lastly, the output signal at timestep t given by Eq. (6) is obtained by repeatedly acting the quantum circuit on the initial state $\rho_0 = |0\rangle\langle 0|$ as

$$\rho_t = \mathcal{T}_{u_t} \circ \mathcal{T}_{u_{t-1}} \circ \cdots \circ \mathcal{T}_{u_1}(\rho_0) \quad (10)$$

and then measuring ρ_t in the computational basis, as shown in Fig. 2. In the experiment, we took 8,192 measurement shots for each t to calculate the mean $\text{Tr}(Z_i \rho_t)$ in Eq. (6).

3 Results & Discussion

Here we show the result of experiment to test the performance of our QRC scheme. We consider two temporal information processing tasks; regression for the NARMA dynamics (NARMA task) and classification

of different objects based on the sensor-data obtained by grabbing them (object classification task). We use two IBM superconducting quantum processors; Melbourne and Toronto devices, whose configurations are illustrated in Fig. 3. Also, in the Qiskit package that we used for the experiments to work with the IBM quantum processors, users can determine the “optimization level” of the quantum circuit transpiler for reducing the noises caused by, e.g., the redundant gate operations. In the QRC scenario, we are rather interested in introducing the noise, hence the optimization level was chosen to be zero (i.e., the noise was not reduced).

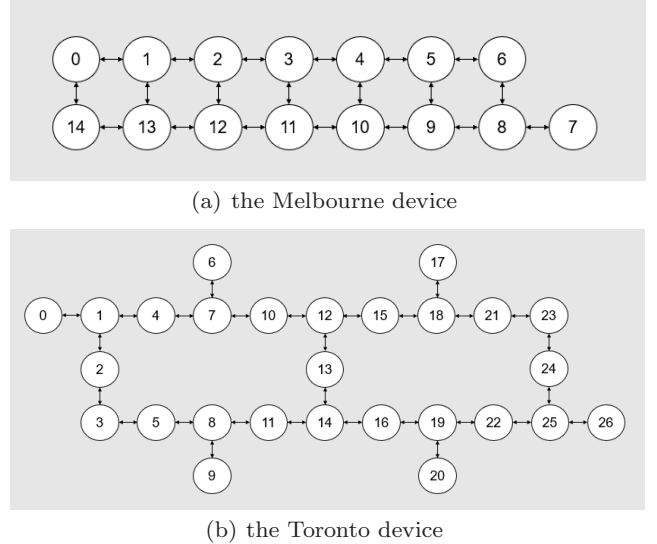


Fig. 3 Configuration of the NISQ devices used for the experiments, (a) the Melbourne device and (b) the Toronto device. In the figures, the nodes and edges represent qubits and the physical coupling of qubits, respectively, where the numbers on the nodes are just labels.

3.1 NARMA task

We firstly demonstrate the performance of our QR systems for the NARMA task. The NARMA task is a benchmark test used to evaluate the performance of dynamical model for temporal information processing, in terms of the nonlinearity and memory (dependency on the past output) properties [45, 46]. The goal of the task is to emulate the dynamics generating the NARMA output sequence $\{y_t\}_{t=1}^M$. An example studied in [22, 47] is described as

$$y_{t+1} = 0.4y_t + 0.4y_{t-1} + 0.6u_t^3 + 0.1, \quad (11)$$

where u_t and y_t are the input and target output sequences, respectively. Another NARMA dynamics stud-

ied in [22, 29, 47] is expressed as

$$y_{t+1} = \alpha y_t + \beta y_t \left(\sum_{j=0}^{n_o-1} y_{t-j} \right) + \gamma u_{t-n_o+1} u_t + \delta, \quad (12)$$

where $(\alpha, \beta, \gamma, \delta) = (0.3, 0.05, 1.5, 0.1)$ and n_o is the order that determines the degree of the nonlinearity. In our experiment, we consider the following three NARMA dynamics; NARMA of Eq. (11) (we call NARMA2), and NARMA5 of Eq. (12) with $n_o = 5$ and $n_o = 10$ (we call NARMA5 and NARMA10, respectively). Note that the number in the task name (e.g., 5 in "NARMA5") implies the order of the nonlinearity, and hence these three NARMA tasks can be used to evaluate the nonlinearity of the QR systems.

As for the input $\{u_t\}_{t=1}^M$, we use the following time series for all the NARMA tasks;

$$u_t = 0.1 \left(\sin \left(\frac{2\pi\bar{\alpha}t}{T} \right) \sin \left(\frac{2\pi\bar{\beta}t}{T} \right) \sin \left(\frac{2\pi\bar{\gamma}t}{T} \right) + 1 \right), \quad (13)$$

with $(\bar{\alpha}, \bar{\beta}, \bar{\gamma}, T) = (2.11, 3.73, 4.11, 100)$, which is used in [22]. Here, we set the length of inputs and outputs to $M = 100$, where the first 10 timesteps are used for washout, the following 70 timesteps are used for training, and the remaining 20 timesteps are used for testing. The washout period is necessary for the QR system to lose the dependency on the initial state ρ_0 , and thus the signals in this period are not used for the training. Figure 4 shows the inputs and the target output sequences for each NARMA task.

We use the Melbourne and Toronto devices for running the unitary operator given in Eqs. (8) and (9) with $a = 2$. These devices are used in the same condition to compare the effect of the hardware-specific noises. In particular, we explore if increasing the system size (accordingly the number of output signals) may improve the performance of QRC, which was numerically predicted in [22]. For this purpose, we study the cases where the number of qubits is chosen as $n = 8, 10$, and 12 ; this means that the number of 2-qubits subsystems is $m = 4, 5$, and 6 , respectively. The qubits used are shown in Fig. 5.

To quantitatively evaluate the performance of the QRC, we calculate the normalized mean squared errors (NMSE) between the output (2), $\bar{y}_t = W_{out} h(x_t)$, and the target output y_t for the testing period, which is expressed as

$$NMSE = \frac{\sum_{t=81}^{100} (\bar{y}_t - y_t)^2}{\sum_{t=81}^{100} y_t^2}. \quad (14)$$

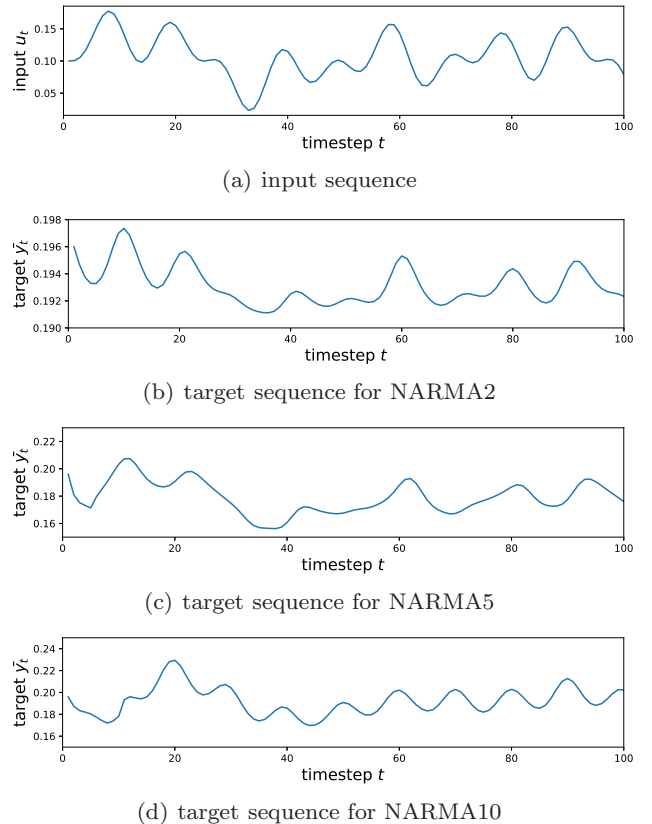


Fig. 4 Time series data used for the experiment. (a) shows the input sequence. (b), (c), and (d) show the target sequences for NARMA2, NARMA5, and NARMA10, respectively.

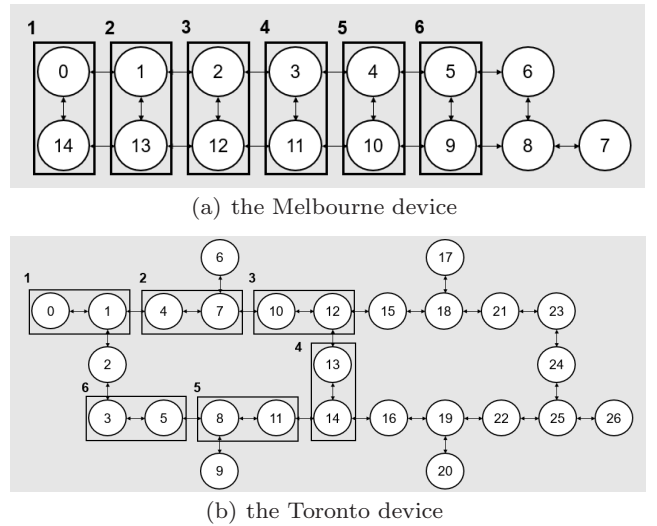


Fig. 5 Qubits that constitute the subsystems in (a) Melbourne device and (b) Toronto device. The black box indicates the subsystem with labels from 1 to 6. When we mention " m subsystems are used", this means that the subsystems labeled 1 to m are used.

Table 1 List of NMSEs for (a) NARMA2, (b) NARMA5, and (c) NARMA10. The bold script means the best NMSE for each NARMA task.

(a) NARMA2							
	Melbourne device			Toronto device			LR
	4-subsystems	5-subsystems	6-subsystems	4-subsystems	5-subsystems	6-subsystems	
Mean	1.3×10^{-5}	1.3×10^{-5}	8.9×10^{-6}	2.9×10^{-5}	2.5×10^{-5}	2.2×10^{-5}	1.8×10^{-5}
Std	6.3×10^{-5}	2.8×10^{-6}	2.8×10^{-6}	6.7×10^{-6}	1.3×10^{-5}	4.1×10^{-6}	—

(b) NARMA5							
	Melbourne device			Toronto device			LR
	4-subsystems	5-subsystems	6-subsystems	4-subsystems	5-subsystems	6-subsystems	
Mean	1.3×10^{-3}	1.3×10^{-3}	1.3×10^{-3}	2.7×10^{-3}	2.2×10^{-3}	1.9×10^{-3}	2.6×10^{-3}
Std	6.7×10^{-4}	4.0×10^{-4}	5.3×10^{-4}	9.6×10^{-4}	2.1×10^{-4}	3.7×10^{-4}	—

(c) NARMA10							
	Melbourne device			Toronto device			LR
	4-subsystems	5-subsystems	6-subsystems	4-subsystems	5-subsystems	6-subsystems	
Mean	1.9×10^{-3}	2.1×10^{-3}	2.0×10^{-3}	3.6×10^{-3}	3.1×10^{-3}	2.3×10^{-3}	9.7×10^{-4}
Std	4.8×10^{-4}	6.0×10^{-4}	3.5×10^{-4}	8.5×10^{-4}	1.2×10^{-3}	5.3×10^{-4}	—

Table 1 summarizes the NMSE for each experimental setting, where the NMSEs are averaged over 10 experimental trials under the same conditions. The experiments had been performed during the period between Aug. 16th and Nov. 2nd in 2020. To see the effect of nonlinearity induced by the QR systems, we compare our model with a simple linear regression (LR) model that predicts the output by $\bar{y}_{t+1} = wu_t + b_0$ with optimized parameters w and b_0 . Also Figs. from 11 to 13 show the result for each NARMA task. Below we list the summary of the results, depending on the type of task.

- For NARMA2 task, all the QR systems on the Melbourne device outperform the LR model. In particular, a larger QR system shows higher performance; in fact, the QR with 6 subsystems show the lowest NMSE among all models. On the other hand, every QR system on the Toronto device is inferior to the LR model.
- We find a similar tendency for NARMA5 task; all the QR systems on the Melbourne device are better than the LR model. However, the performance of the QR system is not improved even by increasing the system size in this task. On the other hand, for the QR systems on the Toronto device, the performances of QRs with 5 or 6 subsystems are higher than the LR model; also the larger system shows a better performance.
- As for NARMA10 task, the QR systems on both Melbourne and Toronto devices cannot outperform the LR model. Also, the tendency with respect to the system size differs from the cases of NARMA2 and NARMA5; the performance improves when in-

creasing the system size for the Toronto device, whilst that of Melbourne device does not improve.

These results show that the performance of our QRC scheme heavily depends on the device; the Melbourne device is always better than the Toronto device for the tasks with the same experimental setting. Also, we find the different tendency of these devices with respect to the number of subsystems. Namely, the performance of the Toronto device is monotonously improved by increasing the system size for all the NARMA tasks, while the Melbourne device does not show such tendency, except for the NARMA2 task.

These device-dependent features can be partly explained by analyzing the output signals from the QR systems. In the analysis, we focus on the the *stationarity* of the output signals; broadly speaking, the stationarity is a notion that represents the time-consistent property of time-series data. Here, to see the stationarity of output signals from the devices, we calculate their mean and variance over the training and testing phase, which are summarized in Fig. 6 and Fig. 7, respectively. From Fig. 6, we observe that, for the case of the Melbourne device, the mean values of the output signals over the training and testing phase are relatively close for every qubit, meaning that the output signals are stationary in view of the mean. On the other hand, some qubits on the Toronto device (say, qubits labeled 0 and 1) witnessed the large gap in the mean value between the training and test phase, implying that the output signals are not in stationary. Further, the unstationarity for the Toronto device can also be seen in view of the variance; that is, in Fig. 7, although both devices experience the decrease of the variance when changing

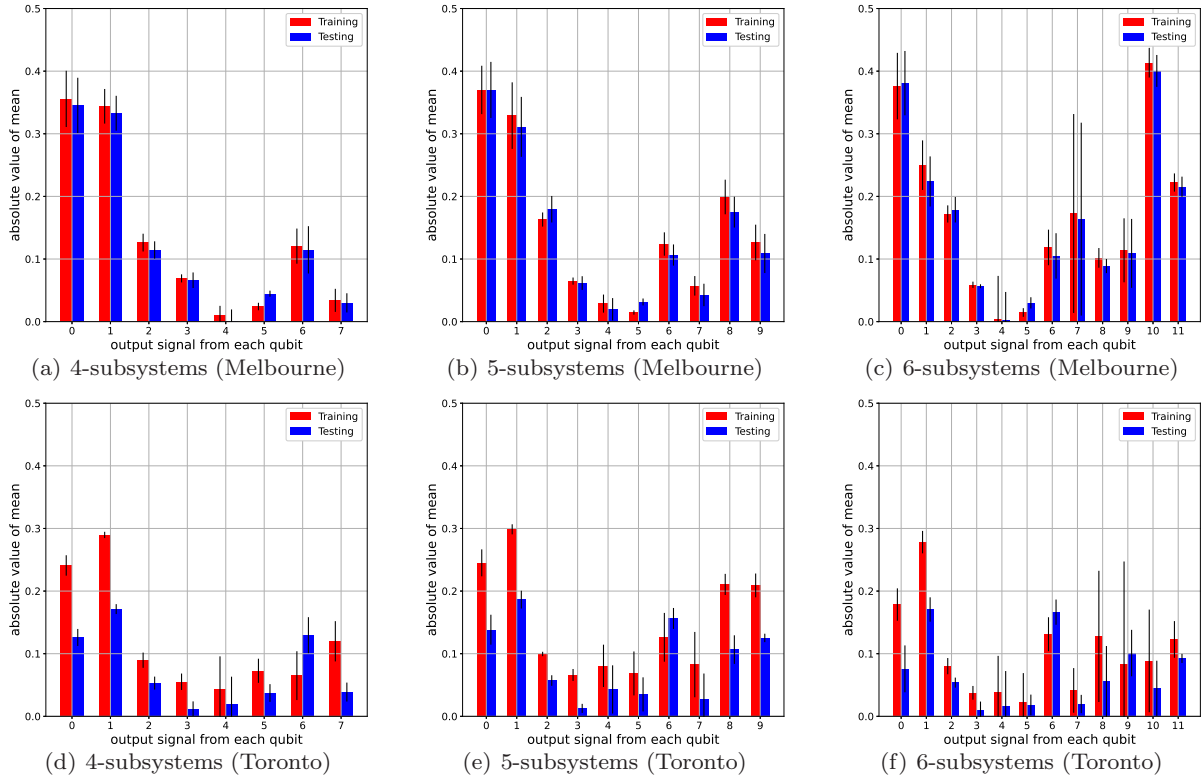


Fig. 6 Mean of the output signal from each qubit over training (red) and test (blue) phase. Note that we here show the absolute value of the mean for the sake of the convenience. The number on the horizontal axis indicates the label of the qubit from which the signal is measured. The upper three panels (a, b, c) and lower three panels (d, e, f) show the results for the Melbourne and Toronto device, respectively.

the phase, the gap for the Toronto device is more significant. (Note that a logarithmic scale is used for the vertical axis of the plots in Fig. 7.) As a consequence, for the Toronto device, the output signals used for training are so different from those in the testing phase, which might be one reason why the Toronto device is inferior to the Melbourne. Also, because the target output for every NARMA tasks is stationary in terms of both the mean and the variance, as shown in Table 2, the unstationary dynamics of Toronto device cannot well track the target, which is also one reason of the inferior performance.

The above-mentioned difference in the stationarity may be attributed to the magnitude of noise; that is, the bigger noise would make the convergence of the dynamics faster and, as a result, lead to a more stationary signal. In fact, presumably the Melbourne device is subjected to a bigger noise than the case of Toronto, due to the difference of the configuration of qubits on the devices. Now, in general, a device with more dense qubit configuration suffers from bigger noise. In this sense, from Fig. 5, it is reasonable that the Melbourne device with dense lattice structure suffers from the effect of

the noise more than the Toronto device with the sparse hexagonal structure. From this standpoint, we can also understand another device-dependent feature regarding the relation between the performance and the system size; the powerful noise on the Melbourne device results in the stationary output signals that are though lacking of the higher order time series. Then, the extra output signals coming from the added system may have little contribution to the performance improvement; on the other hand, output signals generated from the Toronto device have higher-order time series due to the moderate noise, which as a result improves the performance as we increase the system size. In this way, our scheme shows the different performance depending on the hardware, even if the operations (i.e. the type of quantum circuits) are the same. Therefore, it is critical to investigate what kind of noises on quantum hardware are preferable for our scheme, which is left as a future work.

3.2 Object classification task

Next we show the performance of our QR systems for the task of classifying different objects, using the time

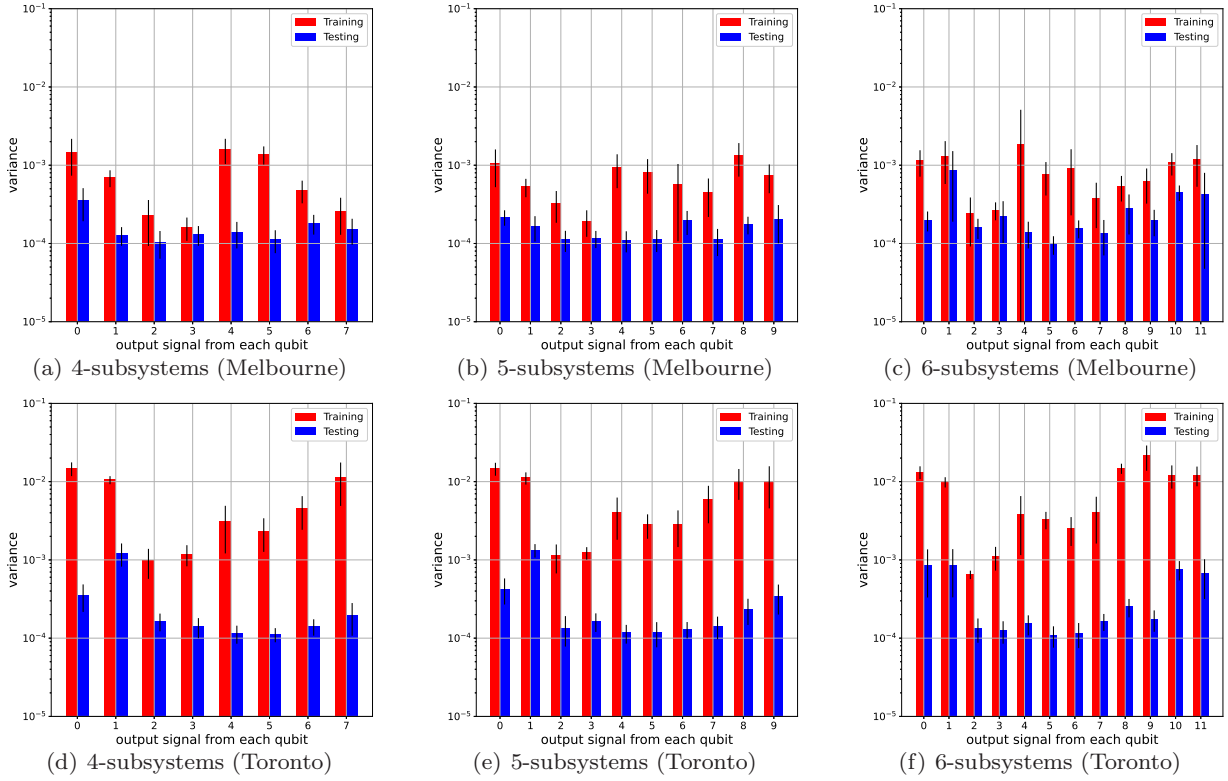


Fig. 7 Variance of the output signal from each qubit over training (red) and test (blue) phase. The number on the horizontal axis indicates the label of the qubit from which the signal is measured. The upper three panels (a, b, c) and lower three panels (d, e, f) show the results for the Melbourne and Toronto device, respectively.

Table 2 Mean and Variance of the target output sequence for (a) training and (b) testing phase.

(a) Training phase			
	NARMA2	NARMA5	NARMA10
Mean	0.193	0.178	0.192
Variance	1.71×10^{-6}	1.61×10^{-4}	1.74×10^{-4}
(b) Testing phase			
	NARMA2	NARMA5	NARMA10
Mean	0.193	0.182	0.197
Variance	9.14×10^{-7}	4.35×10^{-5}	6.46×10^{-4}

series data generated from the sensor robot that grabs them. This task is equivalent to identifying the class to which the time series data belongs. Hence QR system aims to separate different types of those inputs.

We use the linear regression technique to train the readout weight $W_{out} \in \mathbb{R}^{N+1} \times \mathbb{R}^K$, where N is the number of observed signals from the reservoir state and K is the number of classes. Recall that an additional dimension for W_{out} (i.e. “+1” in \mathbb{R}^{N+1}) comes from the extra bias term. To learn the parameters, we simply solve the following linear equation by the pseudo

inverse:

$$(\mathbf{Y}_1, \dots, \mathbf{Y}_{N_{train}}) = W_{out}^T (\tilde{\mathbf{X}}_1, \dots, \tilde{\mathbf{X}}_{N_{train}}), \quad (15)$$

where $\tilde{\mathbf{X}}_i = (\tilde{h}(\mathbf{x}_{t_s}^i), \dots, \tilde{h}(\mathbf{x}_{t_e}^i))$ and $\mathbf{Y}_i = (\bar{y}^i, \dots, \bar{y}^i)$. Here \mathbf{x}_t^i represents the reservoir state at timestep t , and \bar{y}^i does the target output for the i -th training data with the total number of the training data N_{train} . Also t_s and t_e represent the first and last timestep for each data, respectively. The target output is expressed by the one-hot vector (i.e., for example, $[1, 0]^T$ for Object A and $[0, 1]^T$ for object B, for the binary-classification task). As for testing, with the optimized parameter W_{out}^{opt} and $\tilde{\mathbf{X}}_{new} = (\tilde{h}(\mathbf{x}_{t_s}^{new}), \dots, \tilde{h}(\mathbf{x}_{t_e}^{new}))$ for the unseen testing data, we compute the following:

$$t_{new} = \text{argmax} \left(\text{mean}_t \left(W_{out}^{opt T} \tilde{\mathbf{X}}_{new} \right) \right). \quad (16)$$

In fact, t_{new} shows the index of the maximum value in the predicted one-hot vector averaged over the used timesteps (i.e. the period between time t_s and t_e), and thus indicates the class of the data (indeed, this is equivalent to the Winner-Takes-All strategy). Note that this learning method was employed for the classification task with the RC model, for example, in [48, 49].

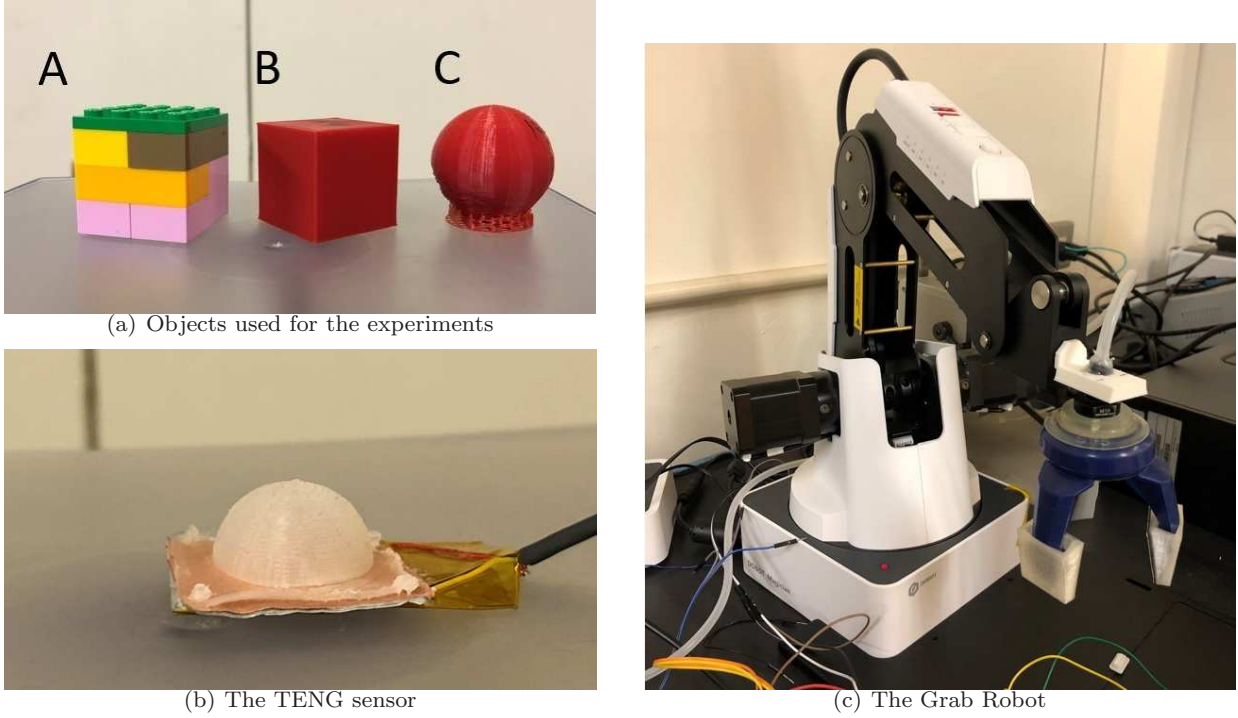


Fig. 8 The objects and an instrument used to collect the sensor-data for the classification tasks. Here, the sensor data of three objects (Panel (a)) are obtained using the TENG sensor (Panel (b)), which is manipulated by the grab robot (Panel (c)).

In this experiment, the following three objects were used; the first object was a cube made of ABS LEGO blocks weighing 15 grams and measuring 3.2 cm wide (Object A) and the remaining two were polylactic acid (PLA) cube and sphere made using a 3D printer with equal widths of 3 cm (Object B and object C, respectively). The picture of these objects are shown in Fig. 8(a). The sensor data of these objects was obtained by grabbing them using the triboelectric nanogenerator (TENG) sensor and the grab robot, illustrated in Figs. 8(b) and 8(c), respectively. The TENG sensor is a pressure sensor which uses an electronegative silicone bubble shaped dome and an electropositive nylon layer as the active materials. Fig. 9 shows the raw time series data for each object, where the grabbing process was repeated for 25 cycles. We here used 20 pieces of a time-series data obtained in one cycle (90 timesteps) for each object, and pre-process the data in the following way;

$$u_t = u'_{t+1} - u'_t, \quad (17)$$

where u_t and u'_t represent the pre-processed and the raw data at time t , respectively. Note that the pre-processing is just taking a finite difference of u'_t , and thus its computational cost is negligible.

In this experiment, we consider four classification tasks; three binary classification tasks (A vs. B, A vs. C, and B vs. C) and a three-class classification task (A

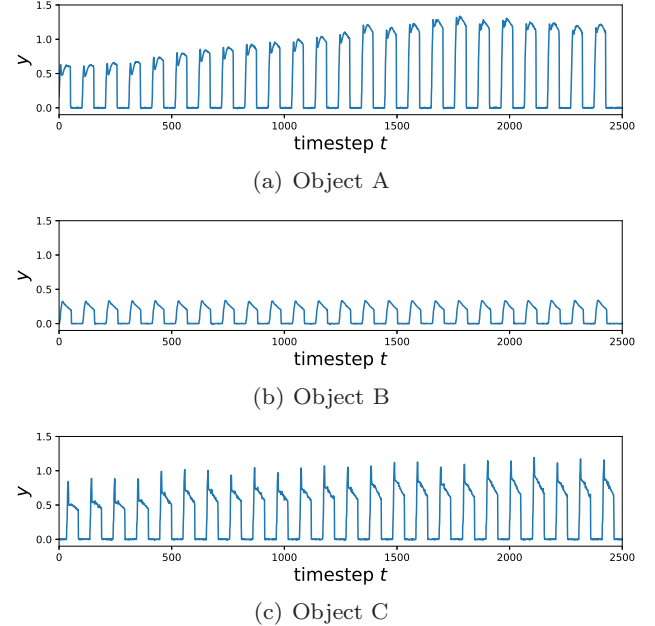


Fig. 9 The raw data of each object. (a) Object A, (b) Object B and (c) Object C.

vs. B vs. C). For all these tasks, we performed 10-fold cross validation to evaluate the performance via the averaged classification accuracy. As for our QR system, we used the 4-subsystems on the Toronto device (subsys-

Table 3 Classification accuracy of our QR system and a simple linear regression model for all classification tasks.

(a) Our QR system			
A vs. B	A vs. C	B vs. C	A vs. B vs. C
Mean	0.90	1.00	1.00
Std	0.20	0.00	0.00
(b) Linear regression			
A vs. B	A vs. C	B vs. C	A vs. B vs. C
Mean	1.00	0.90	1.00
Std	0.00	0.20	0.00

tems labeled 1 to 4 in Fig. 5) with the same unitary operators in Eq. 9, where we set $a = \pi$. Also, for each data, we discard first 40 timestep for washout and the remaining 49 timesteps are used for the learning, i.e. $t_s = 41$, $t_e = 89$. Note that the experiments have been performed during the period between Feb. 22th 2021 and Feb. 23th 2021.

The classification accuracies are shown in Table 3, where we also show the performance of a simple linear classification model to compare the results. Here, the simple linear classifier predicts the class of the data at timestep t by $\bar{y}_t = W_{out}^T u_t + b^T$ with $W_{out}, b \in \mathbb{R}^1 \times \mathbb{R}^K$. We found that our QR system is superior to the linear model for the binary classification task (A vs. C) and the three-class classification, while the linear model is better for the task classifying A and B. Notably, the accuracy of our QR system is almost 0.3 higher than that of the linear model, for the three-class classification task. This result indicates that the QR system can classify three different classes well on the basis of inputs, some classes of which though look similar and may be difficult to categorize. As a matter of fact, the confusion matrix of the linear model in one round of cross-validation (Fig. 10) reveals that Object C in the existence of Objects A and B seems difficult to identify, while our QR systems successfully identify them. Hence this experiment shows that our proposed QR system also has a potential for executing classification tasks.

4 Conclusion

In this work, we propose a QRC scheme that utilizes natural quantum noise; that is, the intrinsic quantum noise, which unavoidably occurs in currently available quantum information devices, is leveraged as a (possibly very rich) computational resource in our QRC framework. We used IBM superconducting quantum processors to experimentally demonstrated the performance of the proposed scheme in two temporal information processing tasks; emulation of the NARMA dy-

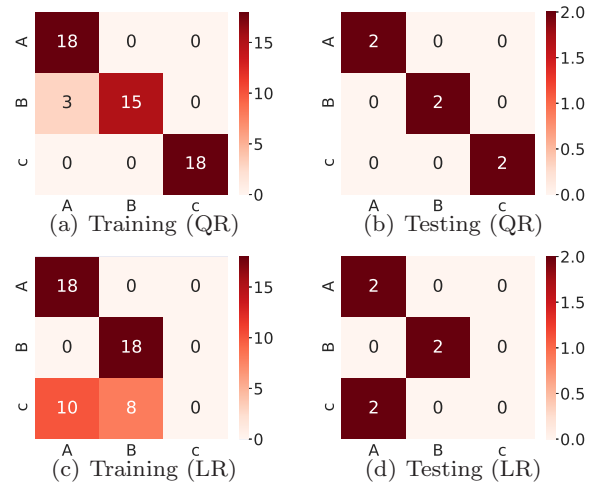


Fig. 10 The confusion matrices for our QR systems and the linear regression (LR) model in one round of cross-validation. The confusion matrices of QR systems (LR model) for training and testing are shown in (c) and (d), respectively.

namics and classification of different objects based on the sensor-data. As a result, we observed that our proposed scheme outperforms a linear regression or classification model for some NARMA tasks and classification tasks.

There are many remaining works to be examined; in particular it is important to improve the performance and the processing speed. To improve the performance, we need to somewhat identify the underlying mechanisms of quantum noise on the device under operation, from the perspective of controllability. In fact, recently we find several quantum system identification methods, which aim to elucidate the complex quantum noises such as crosstalk [43, 44]. These analysis will help us to design a quantum reservoir system with e.g., suitable configuration of qubits as well as the unitary gate of the subsystems. Reducing the processing speed of our QR scheme is also important; actually processing speed is one of the advantages of physical RC framework against other machine learning architectures [20]. In our experimental setting, we have to run the quantum circuits repeatedly to average the stochastic outcomes and obtain the output signals; that is, for the total timesteps L and the number of required measurement S , we need to run the quantum circuit totally LS times, which is thus time consuming. However, thanks to the recent rapid advance of the quantum hardware, we can now perform the mid-circuit measurements for IBM superconducting processors [50], which generates the output signal only with S running of the circuit, meaning that our RC method is scalable.

Finally note that the proposed QRC scheme is not limited to NISQ. Even in the era of future fault-tolerant quantum computing devices, it is easy to introduce noise by simply relaxing the control level for qubits; then the degree of noise level to be introduced as well as the structure of noise dynamics will be a central topic to be explored.

Acknowledgements This work was supported by MEXT Quantum Leap Flagship Program Grant Number JPMXS0118067285 and JPMXS0120319794, and also JSPS KAKENHI Grant Number 20H05966. YS and NY acknowledge the discussion with Kohei Nakajima and Tran Hoan.

References

1. Baldi, P., Brunak, S., Bach, F.: Bioinformatics: the machine learning approach. MIT press (2001)
2. He, K., Zhang, X., Ren, S., Sun, J.: Deep residual learning for image recognition. In: Proceedings of the IEEE conference on computer vision and pattern recognition, pp. 770–778 (2016)
3. Ronneberger, O., Fischer, P., Brox, T.: U-net: Convolutional networks for biomedical image segmentation. In: International Conference on Medical image computing and computer-assisted intervention, pp. 234–241. Springer (2015)
4. Dixon, M.F., Halperin, I., Bilokon, P.: Machine Learning in Finance. Springer (2020)
5. Mullainathan, S., Spiess, J.: Machine learning: an applied econometric approach. *Journal of Economic Perspectives* **31**(2), 87–106 (2017)
6. Greydanus, S., Dzamba, M., Yosinski, J.: Hamiltonian neural networks. arXiv preprint arXiv:1906.01563 (2019)
7. Hermann, J., Schätzle, Z., Noé, F.: Deep-neural-network solution of the electronic schrödinger equation. *Nature Chemistry* **12**(10), 891–897 (2020)
8. Young, T., Hazarika, D., Poria, S., Cambria, E.: Recent trends in deep learning based natural language processing. *IEEE Computational Intelligence magazine* **13**(3), 55–75 (2018)
9. Schaal, S., Atkeson, C.G.: Learning control in robotics. *IEEE Robotics & Automation Magazine* **17**(2), 20–29 (2010)
10. Mandic, D., Chambers, J.: Recurrent neural networks for prediction: learning algorithms, architectures and stability. Wiley (2001)
11. Jaeger, H., Haas, H.: Harnessing nonlinearity: Predicting chaotic systems and saving energy in wireless communication. *science* **304**(5667), 78–80 (2004)
12. Jaeger, H.: The “echo state” approach to analysing and training recurrent neural networks-with an erratum note. Bonn, Germany: German National Research Center for Information Technology GMD Technical Report **148**(34), 13 (2001)
13. Maass, W., Natschläger, T., Markram, H.: Real-time computing without stable states: A new framework for neural computation based on perturbations. *Neural computation* **14**(11), 2531–2560 (2002)
14. Bishop, C.M.: Pattern recognition and machine learning. Springer (2006)
15. Schrauwen, B., D’Haene, M., Verstraeten, D., Van Campenhout, J.: Compact hardware liquid state machines on fpga for real-time speech recognition. *Neural networks* **21**(2-3), 511–523 (2008)
16. Fernando, C., Sojakka, S.: Pattern recognition in a bucket. In: European conference on artificial life, pp. 588–597. Springer (2003)
17. Nakajima, K., Hauser, H., Li, T., Pfeifer, R.: Information processing via physical soft body. *Scientific reports* **5**(1), 1–11 (2015)
18. Caluwaerts, K., Despraz, J., İşçen, A., Sabelhaus, A.P., Bruce, J., Schrauwen, B., SunSpiral, V.: Design and control of compliant tensegrity robots through simulation and hardware validation. *Journal of the royal society interface* **11**(98), 20140520 (2014)
19. Torrejon, J., Riou, M., Araujo, F.A., Tsunegi, S., Khalsa, G., Querlioz, D., Bortolotti, P., Cros, V., Yakushiji, K., Fukushima, A., et al.: Neuromorphic computing with nanoscale spintronic oscillators. *Nature* **547**(7664), 428–431 (2017)
20. Tanaka, G., Yamane, T., Héroux, J.B., Nakane, R., Kanazawa, N., Takeda, S., Numata, H., Nakano, D., Hirose, A.: Recent advances in physical reservoir computing: A review. *Neural Networks* **115**, 100–123 (2019)
21. Nakajima, K.: Physical reservoir computing—an introductory perspective. *Japanese Journal of Applied Physics* **59**(6), 060501 (2020)
22. Fujii, K., Nakajima, K.: Harnessing disordered-ensemble quantum dynamics for machine learning. *Physical Review Applied* **8**(2), 024030 (2017)
23. Chen, J., Nurdin, H.I.: Learning nonlinear input–output maps with dissipative quantum systems. *Quantum Information Processing* **18**(7), 1–36 (2019)
24. Chen, J., Nurdin, H.I., Yamamoto, N.: Temporal information processing on noisy quantum computers. *Physical Review Applied* **14**(2), 024065 (2020)
25. Govia, L., Ribeill, G., Rowlands, G., Krovi, H., Ohki, T.: Quantum reservoir computing with a single nonlinear oscillator. *Physical Review Research* **3**(1), 013077 (2021)
26. Martínez-Peña, R., Nokkala, J., Giorgi, G.L., Zambrini, R., Soriano, M.C.: Information processing capacity of spin-based quantum reservoir computing systems. *Cognitive Computation* pp. 1–12 (2020)
27. Nakajima, K., Fujii, K., Negoro, M., Mitarai, K., Kitagawa, M.: Boosting computational power through spatial multiplexing in quantum reservoir computing. *Physical Review Applied* **11**(3), 034021 (2019)
28. Kutz, A., Fujii, K., Sagawa, T.: Optimizing a quantum reservoir computer for time series prediction. *Scientific reports* **10**(1), 1–7 (2020)
29. Tran, Q.H., Nakajima, K.: Higher-order quantum reservoir computing. arXiv preprint arXiv:2006.08999 (2020)
30. Ghosh, S., Opala, A., Matuszewski, M., Paterek, T., Liew, T.C.: Reconstructing quantum states with quantum reservoir networks. *IEEE Transactions on Neural Networks and Learning Systems* (2020)
31. Tran, Q.H., Nakajima, K.: Learning temporal quantum tomography. arXiv preprint arXiv:2103.13973 (2021)
32. Negoro, M., Mitarai, K., Fujii, K., Nakajima, K., Kitagawa, M.: Machine learning with controllable quantum dynamics of a nuclear spin ensemble in a solid. arXiv preprint arXiv:1806.10910 (2018)
33. Preskill, J.: Quantum computing in the nisq era and beyond. *Quantum* **2**, 79 (2018)
34. Jaeger, H.: Adaptive nonlinear system identification with echo state networks. *Advances in neural information processing systems* **15**, 609–616 (2002)

35. Verstraeten, D., Schrauwen, B., Stroobandt, D., Van Campenhout, J.: Isolated word recognition with the liquid state machine: a case study. *Information Processing Letters* **95**(6), 521–528 (2005)
36. Buehner, M., Young, P.: A tighter bound for the echo state property. *IEEE Transactions on Neural Networks* **17**(3), 820–824 (2006)
37. Meurer, T., Graichen, K., Gilles, E.D.: Control and observer design for nonlinear finite and infinite dimensional systems, vol. 322. Springer Science & Business Media (2005)
38. Nielsen, M.A., Chuang, I.: Quantum computation and quantum information (2002)
39. Altafini, C., Ticozzi, F.: Modeling and control of quantum systems: an introduction. *IEEE Transactions on Automatic Control* **57**(8), 1898–1917 (2012)
40. Schirmer, S., Wang, X.: Stabilizing open quantum systems by markovian reservoir engineering. *Physical Review A* **81**(6), 062306 (2010)
41. Morris, J., Pollock, F.A., Modi, K.: Non-markovian memory in ibmqx4. arXiv preprint arXiv:1902.07980 (2019)
42. Havlíček, V., Córcoles, A.D., Temme, K., Harrow, A.W., Kandala, A., Chow, J.M., Gambetta, J.M.: Supervised learning with quantum-enhanced feature spaces. *Nature* **567**(7747), 209–212 (2019)
43. Sarovar, M., Proctor, T., Rudinger, K., Young, K., Nielsen, E., Blume-Kohout, R.: Detecting crosstalk errors in quantum information processors. *Quantum* **4**, 321 (2020)
44. Winick, A., Wallman, J.J., Emerson, J.: Simulating and mitigating crosstalk. arXiv preprint arXiv:2006.09596 (2020)
45. Hochreiter, S., Schmidhuber, J.: Long short-term memory. *Neural computation* **9**(8), 1735–1780 (1997)
46. Kubota, T., Nakajima, K., Takahashi, H.: Dynamical anatomy of narma10 benchmark task. arXiv preprint arXiv:1906.04608 (2019)
47. Atiya, A.F., Parlos, A.G.: New results on recurrent network training: unifying the algorithms and accelerating convergence. *IEEE transactions on neural networks* **11**(3), 697–709 (2000)
48. Araujo, F.A., Riou, M., Torrejon, J., Tsunegi, S., Querlioz, D., Yakushiji, K., Fukushima, A., Kubota, H., Yuasa, S., Stiles, M.D., et al.: Role of non-linear data processing on speech recognition task in the framework of reservoir computing. *Scientific reports* **10**(1), 1–11 (2020)
49. Larger, L., Baylón-Fuentes, A., Martinenghi, R., Udaltssov, V.S., Chembo, Y.K., Jacquot, M.: High-speed photonic reservoir computing using a time-delay-based architecture: Million words per second classification. *Physical Review X* **7**(1), 011015 (2017)
50. Mid-circuit measurements tutorial. <https://quantum-computing.ibm.com/lab/docs/ql/manage/systems/midcircuit-measurement/> (Accessed: 2021-05-11)

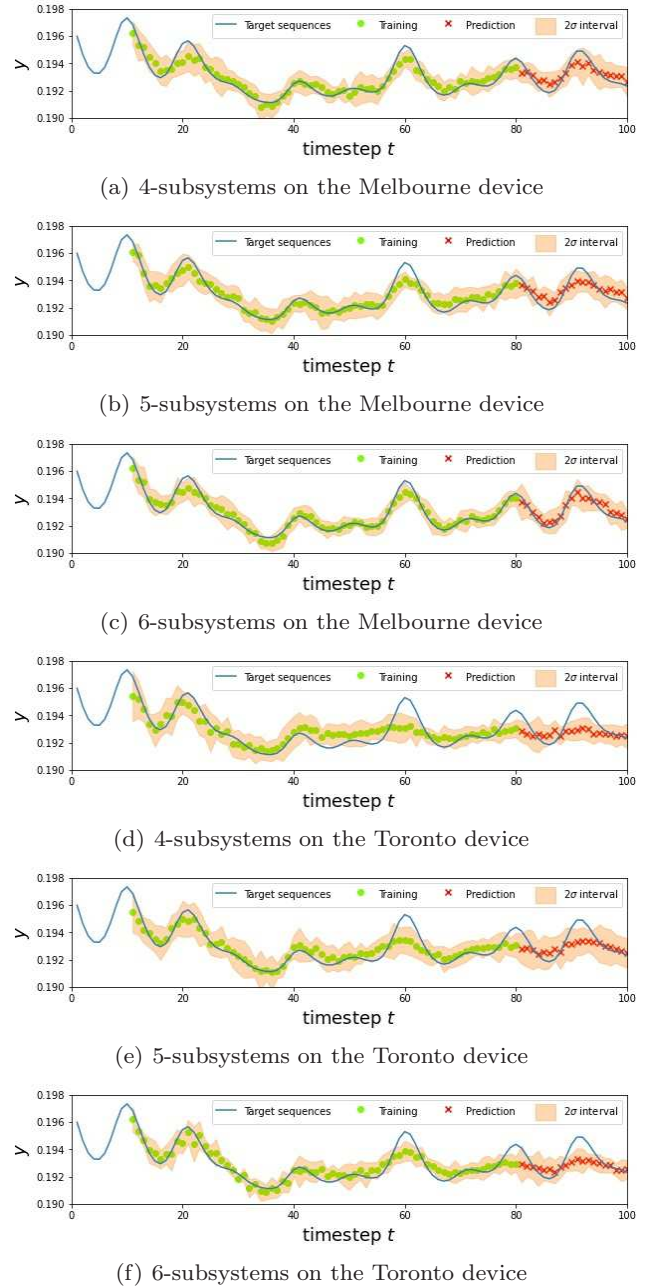
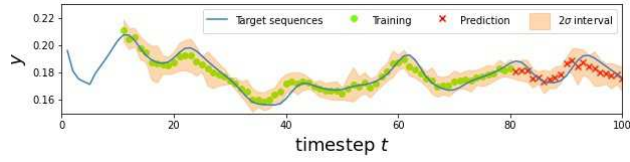
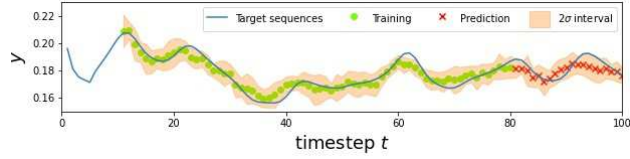


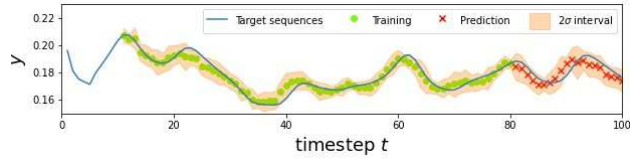
Fig. 11 The result for NARMA2 using different QR systems. In the figures, the blue line represents the targets, green circles and red crosses are the predictions in the training and testing phase, respectively, and the blur orange regions are 2σ intervals.



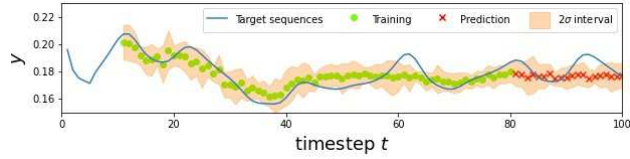
(a) 4-subsystems on the Melbourne device



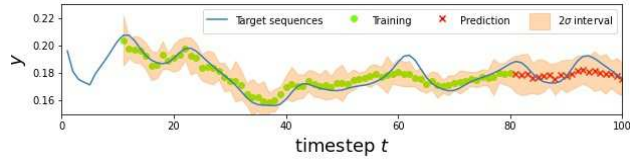
(b) 5-subsystems on the Melbourne device



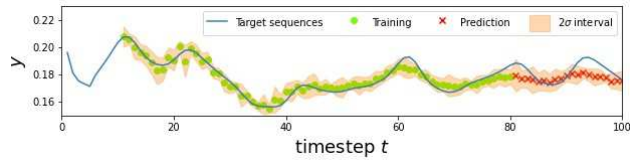
(c) 6-subsystems on the Melbourne device



(d) 4-subsystems on the Toronto device

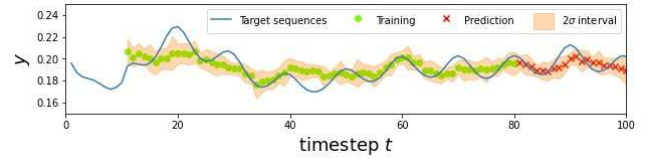


(e) 5-subsystems on the Toronto device

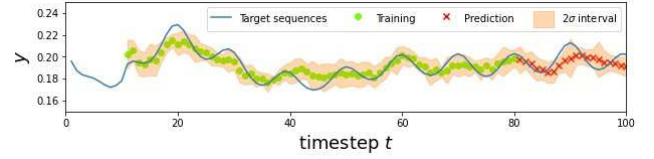


(f) 6-subsystems on the Toronto device

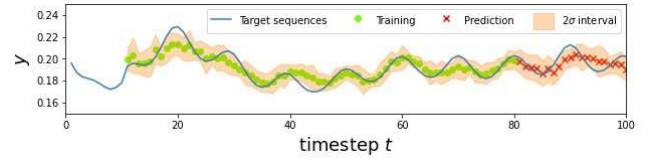
Fig. 12 The result for NARMA5 using different QR systems. In the figures, the blue line represents the targets, green circles and red crosses are the predictions in the training and testing phase, respectively, and the blur orange regions are 2σ intervals.



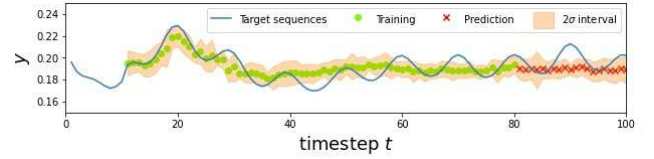
(a) 4-subsystems on the Melbourne device



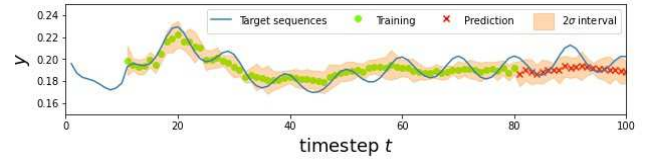
(b) 5-subsystems on the Melbourne device



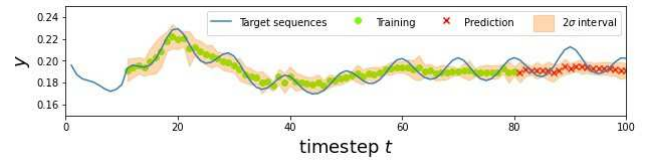
(c) 6-subsystems on the Melbourne device



(d) 4-subsystems on the Toronto device



(e) 5-subsystems on the Toronto device



(f) 6-subsystems on the Toronto device

Fig. 13 The result for NARMA10 using different QR systems. In the figures, the blue line represents the targets, green circles and red crosses are the predictions in the training and testing phase, respectively, and the blur orange regions are 2σ intervals.